

Development and Application of a ReaxFF Reactive Force Field for Ni-Doped MoS₂

Karen Mohammadtabar,[†] Enrique Guerrero,[‡] Sergio Romero Garcia,[†] Yun
Kyung Shin,[¶] Adri C. T. van Duin,[¶] David A. Strubbe,[‡] and Ashlie Martini^{*,†}

[†]*Department of Mechanical Engineering, University of California Merced, 5200 N. Lake
Road, Merced, California 95343, United States*

[‡]*Department of Physics, University of California Merced, 5200 N. Lake Road, Merced,
California 95343, United States*

[¶]*Department of Mechanical Engineering, Pennsylvania State University, University Park,
Pennsylvania 16802, United States*

E-mail: amartini(at)ucmerced.edu

Abstract

The properties of MoS₂ can be tuned or optimized through doping. In particular, Ni doping has been shown to improve the performance of MoS₂ for various applications, including catalysis and tribology. To enable investigation of Ni-doped MoS₂ with reactive molecular dynamics simulations, we developed a new ReaxFF force field to describe this material. The force field parameters were optimized to match a large set of density-functional theory (DFT) calculations of 2H-MoS₂ doped with Ni, at four different sites (Mo-substituted, S-substituted, octahedral intercalation, and tetrahedral intercalation), under uniaxial, biaxial, triaxial, and shear strain. The force field was evaluated by comparing ReaxFF- and DFT-relaxed structural parameters, the tetrahedral/octahedral energy difference in doped 2H, energies of doped 1H and 1T monolayers, and doped 2H structures with vacancies. We demonstrated the application of the force field with reactive simulations of sputtering deposition and annealing of Ni-doped MoS₂ films. Results show that the developed force field can successfully model the phase transition of Ni-doped MoS₂ from amorphous to crystalline. The newly developed force field can be used in subsequent investigations to study the properties and behavior of Ni-doped MoS₂ using reactive molecular dynamics simulations.

Introduction

Molybdenum disulfide (MoS₂) is a transition metal dichalcogenide with a layered structure where each layer consists of molybdenum atoms sandwiched between sulfur atoms. Three main applications of the material are in catalysis, opto-electronics, and tribology. The chemically active edges of MoS₂ nanoparticles have been used to catalyze various reactions, including, hydrogen evolution,¹ hydrotreatment of oil,² and pollutant removal.^{3,4} In 2D form, MoS₂ is widely used as a catalyst for hydrogen evolution reactions⁵⁻⁷ and CO₂ reduction.⁸⁻¹¹ In opto-electronics, single-layer MoS₂ is a semiconductor with a direct band gap that can be used to construct high efficiency transistors.^{12,13} MoS₂ can be synthesized by chemical vapor

deposition to form large-area monolayers for use as atomically thin optical and photovoltaic devices.¹⁴ In tribology, the weak van der Waals forces between layers provide low shear resistance, making MoS₂ an effective low-friction solid lubricant or, in nanoparticle form, a liquid lubricant additive.^{15–18}

MoS₂ can be doped to enhance its properties.¹⁵ Many different elements have been explored as possible MoS₂ dopants, particularly transition metals.^{15,19,20} Dopants can provide various benefits, including altering the band gap,²¹ catalytic reactivity,²² hardness,²³ and nanoscale friction.²⁴ Here, we focus on Ni dopants, which have been shown to improve the performance of MoS₂ for various applications.^{2,25,26} DFT simulations have found four metastable sites for a Ni dopant atom in the 2H-MoS₂ crystallographic structure.²⁷ Dopants can replace an Mo or an S atom in the crystal structure, or they can be intercalated between MoS₂ layers, either between a sulfur site in one layer and a molybdenum site in the other layer (tetrahedral with 4 Ni–S bonds), or between hexagonal holes in both layers (octahedral with 6 Ni–S bonds).²⁸

Studies have investigated the atomistic structure of Ni-doped MoS₂ as well as its electronic and tribological properties. In doped MoS₂ nano-clusters, the Ni dopant was reported to substitute Mo atoms at edge sites leading to truncation of the cluster morphology relative to un-doped MoS₂.¹⁹ Conversely, Ni doping has also been found to enhance MoS₂ crystal size by increasing the mobility of edge planes during crystallization.²⁹ It has been observed that Ni doping can also transform the 2H-MoS₂ structure to the metallic 1T phase.^{30,31}

Studies have shown that Ni doping increases the number of active sites which, in turn, improves the catalytic performance of MoS₂ in reduction of graphene oxide,³² gas sensing,²⁰ and hydrogen evolution and production.^{25,33–35} Ni also increases the S-vacancy defect density,³⁶ resulting in better catalytic activity for hydrogen evolution reaction.³⁷ Ni doping changes the electronic properties of MoS₂:^{37–39} specifically, doping enhances the low electrical conductivity of MoS₂, making this material a promising candidate for electronic applications such as batteries.^{40,41} In tribology, it has been shown that MoS₂ films co-sputtered with Ni

compare favorably to un-doped MoS₂ in terms of friction, wear, and useful life of mechanical parts.^{23,42–44} The improvement in the tribological performance of MoS₂ is particularly notable at low temperatures, which makes Ni-doped MoS₂ ideal as a solid lubricant for space applications where performance at extreme conditions is critical.^{45,46}

Ni-doped MoS₂ has been studied using *ab initio* density functional theory (DFT) calculations. Such calculations have shown that the activity of edge sites is doubled⁴⁷ and that gas adsorption and sensing is enhanced^{48,49} by Ni. Other studies showed that Ni doping improves the catalytic performance of MoS₂ by decreasing the surface sulfur-metal bonding energy,⁵⁰ as well as weakening the S–H bond strength.⁵¹ Previous DFT-based studies have provided details about structures, bonding, thermodynamics, vibrational properties, elasticity, and interlayer binding in Ni-doped bulk 2H, bulk 3R, and monolayer 1H-MoS₂ in different phases.^{27,28} DFT studies have also examined the energies and structural changes in frictional sliding of Ni-doped 2H and bilayer MoS₂,⁵² and the range of different reconstructed phases accessible by Ni-doping of monolayer 1T-MoS₂.⁵³ However, such calculations are computationally demanding, limiting the time- and size-scales of model systems that can be studied.

An alternative simulation approach is molecular dynamics (MD) based on empirical models, or force fields, that describe the interactions between atoms. Several force fields have been developed, or optimized, for MoS₂. First, a Stillinger-Weber force field was developed for MoS₂ and used to calculate mechanical and thermal properties of single layer MoS₂.^{54,55} However, the force field could not capture the behavior of MoS₂ at states far from equilibrium,⁵⁶ and did not include parameters for interlayer interactions. A custom, interpretable force field compatible with various non-reactive potential formalisms was developed for 2H-MoS₂⁵⁷ as well as for Cr-doped 2H-MoS₂.⁵⁸ Despite accurate representation of energetic, mechanical, and surface properties, these potentials do not model the formation and breaking of chemical bonds. A many-body Mo/S potential based on the Reactive Empirical Bond Order (REBO) and Tersoff potentials was developed for MoS₂.⁵⁹ The force field was able to

reproduce expected lattice constants as well as mechanical properties of MoS₂, but it was unable to accurately model surface energy.

Several force fields within the ReaxFF formalism, that captures the formation and breaking of chemical bonds, have been parameterized for MoS₂ as well.^{56,60-62} These force fields have been used in simulations of crystallization,^{56,60-63} active edge sites,⁶⁴ creation of vacancies,^{56,65,66} distribution and dynamics of defects,⁶⁷ mechanical properties of MoS₂ monolayer heterostructures,⁶⁸⁻⁷⁰ and tribological behavior of multi-layer MoS₂.⁷¹ However, to investigate Ni-doped MoS₂, force field parameters that include the interactions between Ni and MoS₂ are needed, which is a challenge as new interactions are introduced and the dopant's effect on the otherwise weak interlayer interactions must be described.

In this study, two new ReaxFF force fields were developed for Ni-doped MoS₂. The force field parameters were optimized by comparing ReaxFF energies to those obtained from a large set of DFT calculations of the equation of state (energy vs. strain) of Ni-doped 2H-MoS₂ under uniaxial, biaxial, triaxial, and in-plane shear strain. DFT calculations were performed with Ni dopants at each of four different sites: Mo-substituted, S-substituted, octahedral, and tetrahedral intercalation. The resulting ReaxFF force field was evaluated based on relaxed bond lengths and structural parameters in 2H, as well as calculations of structures not in the training set such as doped 1H and 1T monolayers and doped 2H with vacancies as well as sliding. Finally, we applied the new force field to model sputter deposition and annealing of Ni-doped MoS₂, pointing the way to future applications.

Methods

DFT Calculations

As in our previous work on thermodynamics and vibrational properties of Ni-doped MoS₂,²⁷ the plane-wave density functional theory (DFT) code Quantum ESPRESSO⁷² was used for quantum calculations. The Perdew-Burke-Ernzerhof⁷³ (PBE) generalized gradient ap-

proximation was used with Grimme-D2⁷⁴ van der Waals correction, and the electron-ion interaction was described with optimized norm-conserving Vanderbilt pseudopotentials⁷⁵ parametrized by Schlipf and Gygi.⁷⁶ All DFT computations used a kinetic energy cutoff of 60 Ry. PBE + Grimme-D2 has been shown to accurately describe the lattice parameters, elastic constants, and phonon frequencies of MoS₂.²⁷ Ni-doped 2H MoS₂ has been previously computed not to be magnetic,²⁸ so we used non-spin-polarized DFT.

The training set was composed of 2H-MoS₂ in $2 \times 2 \times 1$ supercells, where the third direction is perpendicular to the basal plane of the layers. While there are effects of doping concentration, as studied in detail in Guerrero et al.²⁷, this size of supercell is sufficient to capture the local interactions that the force field must describe. Pristine 2H-bulk structures have six atoms per unit cell; a half-shifted Monkhorst-Pack k -grid of $4 \times 4 \times 4$ was used. In the absence of any available structures from X-ray diffraction, our starting configurations are the relaxed pristine structures with Ni atoms substituted, or intercalated in the high-symmetry tetrahedral or octahedral locations. The structures were relaxed toward zero stress using Quantum ESPRESSO’s standard BFGS algorithm. The relaxation ended when forces and stresses were below thresholds of 10^{-4} Ry/Bohr and 0.1 kbar, respectively. The relaxed lattice parameters of the hexagonal primitive cell are $a = b = 3.19 \text{ \AA}$, $c = 12.40 \text{ \AA}$, $\alpha = \beta = 90^\circ$, and $\gamma = 120^\circ$. The dopant sites were chosen because they are stable or meta-stable;²⁷ other sites such as intralayer interstitial or S-S bridge intercalation would relax to other structures. The stable doped structures (Mo-substituted, S-substituted, and intercalation at the tetrahedral and octahedral sites, shown in Figure 1) were taken from Guerrero et al.²⁷, constructed with one Ni atom in each $2 \times 2 \times 1$ supercell, i.e., up to 12.5% doping (which may be also considered alloying). For validation, defect calculations in $3 \times 3 \times 1$ supercells used a $3 \times 3 \times 4$ k -grid. The training set systems are shown in Figure 1. Due to lower computational efficiency for systems with acute cell angles in the stand-alone ReaxFF code and LAMMPS, the results were used to construct nearly orthorhombic ($\alpha = \beta = \gamma = 90^\circ$) cells with twice the number of atoms and twice the energy, which does not change any

intensive properties. All DFT results compared to ReaxFF are in terms of this doubled cell, for clarity.

Strained 2H-bulk structures were studied under six strain conditions: uniaxial x -strain, uniaxial z -strain, biaxial xy -strain, triaxial strain, and xy -shear. Note that due to exact symmetries in the pristine structure, and approximate symmetries in the doped structures,²⁷ uniaxial y -strain would not provide further distinct information. For each strain direction, seven points were sampled with strains ranging from -15% to 15% in intervals of 5%, consistent with strain ranges in the initial MoS₂ parameterization.⁵⁶ Similarly, shear calculations were performed for seven points with shearing angles (the angle between orthogonal a and b lattice vectors between $\sim 72^\circ$ and 108°). In each case, the atomic forces were relaxed to 10^{-4} Ry/Bohr with fixed lattice vectors.

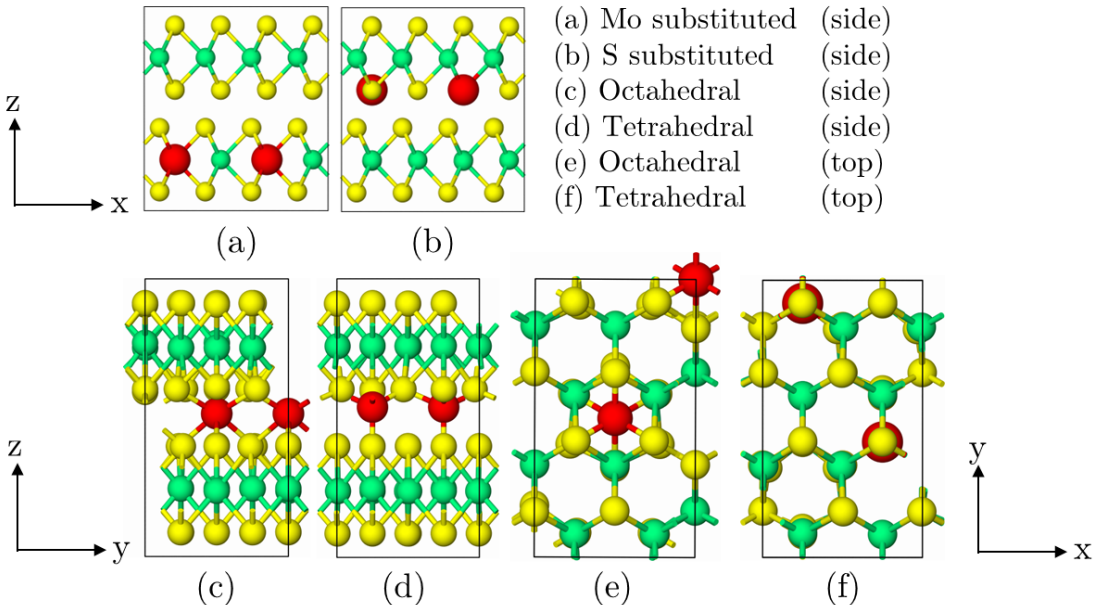


Figure 1: Side views of the training set structures, illustrating the four possible locations of the Ni dopant in MoS₂: (a) Mo-substituted, (b) S-substituted, (c) octahedral intercalation, and (d) tetrahedral intercalation. (e) and (f) show top views of the octahedral and tetrahedral intercalations, respectively. Sphere colors correspond to S (yellow), Mo (green), and Ni (red).

ReaxFF Force Field and Parameterization

ReaxFF is a reactive empirical force field based on bond order and atomic distances that originally was developed for hydrocarbons.⁷⁷ Over the years, many different parameter sets have been developed for various chemical systems. ReaxFF accounts for the contributions of various partial energy terms that enable ReaxFF to accurately model covalent and ionic bonds as well as non-bonded interactions. The total energy in the force field is the sum of the bond energy, over-coordination and under-coordination energy corrections, angle strain, torsion energy, torsion conjugation, van der Waals, and Coulomb energies. A detailed explanation of all terms can be found in the original ReaxFF article.⁷⁷

We started from two different parameter sets that were previously developed for S/Mo interactions, one reported in 2017⁵⁶ and the other reported in 2022.⁶² The 2017 potential was developed specifically for single-layer MoS₂, with a focus on its mechanical response with and without vacancies, and included parameters to model interactions between MoS₂ and oxygen. Then, the 2022 potential was developed by modifying the Mo/S parameters in the 2017 potential to better capture crystallization of MoS₂ in bilayer and bulk form. We introduced Ni parameters for both the 2017 and the 2022 force fields. The Ni metal parameter set employed in this work is the same as that of Ni/Mo force field.⁷⁸ The Ni metal force field, including Ni atom parameters (1-body parameters) and Ni-Ni interactions, was originally developed for Ni-catalyzed hydrocarbon chemistry.⁷⁹ The Ni parameter set was trained against DFT data for the 2017 potential on the equations of states of various crystal phases (fcc, bcc, diamond, A15 and sc), their cohesive energies, and the surface energies for Ni(111) and Ni(100) surfaces. Since the newer study⁶² used bulk MoS₂ DFT training data and was demonstrated for crystallization of MoS₂, which is closer to our goal of simulating deposition, we report the results for the new potential based on the 2022 parameters in the main text. However, comparisons of the training results with the DFT data for the potential based on the 2017 force field (including Ni/S and Mo/Ni training results in Figs. S1-4 and Table S1) as well as both potential files are available as Supporting Information.

Our force field was trained against the DFT data by optimizing the parameters specifically for Mo-S-Ni, S-Mo-Ni, and S-Ni-Mo valence angles. Other parameters, such as those for Ni-S and Mo-Ni bonds, remained fixed to literature values. The bond angle parameters were the equilibrium angle, first and second force constants, undercoordination parameter, and energy/bond order. The process of parameterization included calculating the potential energy of each structure (E^{ReaxFF}) which was then compared to the energy obtained from DFT for the same structure (E^{DFT}). A weighted error was calculated as:

$$\text{Error} = \sum_i \left(\frac{E_i^{\text{ReaxFF}} - E_i^{\text{DFT}}}{w_i} \right)^2 \quad (1)$$

where w_i is the weight associated with each data point on the energy plots. The weights were chosen to prioritize minimizing the difference between the DFT and the ReaxFF energies for near-equilibrium structures. The parameters were optimized by the single-parameter search optimization technique⁸⁰ in the stand-alone ReaxFF package. The energy difference between each strained and equilibrated structure as obtained from ReaxFF and DFT was plotted as a function of strain for each strain direction. The same was done for sheared structures at each shearing angle. The parameterization process was repeated until the shapes of the energy plots were as similar as possible between ReaxFF and DFT. This procedure has been used previously to optimize ReaxFF parameters for various chemical systems.^{56,62,79,81–83} The accuracy of the developed force field was evaluated and it was then used for energy minimization and dynamics simulations with the Large-scale Atomic/Molecular Massively Parallel Simulator (LAMMPS) code.⁸⁴

Results and Discussion

Force Field Parameterization

The energies of all four structures under all five strain conditions were used in the training of the ReaxFF force field. The results for uniaxial straining in the x - and z -directions of the four Ni-doped MoS₂ structures are shown in Figure 2 and Figure 3, respectively. The equation of state energies given are those of the doubled cell, with respect to the energy in each method of the unstrained structure. The structures used in ReaxFF result from a relaxation with fixed cell parameters, starting from the DFT structures.

We can begin by examining the energy difference between unstrained octahedrally and tetrahedrally intercalated structures. While Mo-substituted, S-substituted, and intercalated structures have different stoichiometries and cannot be compared in energy without assumptions about the chemical potential,²⁷ we can directly compare the energies of the two intercalated structures. In DFT, tetrahedral is lower than octahedral in energy by 38.8 kcal/mol in these structures (0.841 eV per Ni atom).²⁷ We find a very close level of agreement in ReaxFF, which gives tetrahedral lower in energy by 41.0 kcal/mol. Note that in referring to energies in kcal/mol in this work we will consistently mean energies *per unit cell*, which in most cases is a 2×2 cell. This agreement is essential for the correct structures to appear in MD simulations, and also demonstrates the ability of our ReaxFF parameterization to describe accurately the energy difference between the 6-bonded octahedral and 4-bonded tetrahedral environment.

The uniaxial ReaxFF energies are in reasonably good agreement with the DFT energies, despite the large strains that were applied. Discrepancies are largest at large strain. Shapes are similar, though for x strain and S-substituted, ReaxFF actually has a minimum shifted to +5% strain (vs the DFT structure), and for z strain and Mo-substituted the minimum is shifted to -5%. For x strain, Mo-substituted has a larger energy value in ReaxFF than in DFT for all strains, whereas in the other cases, ReaxFF is higher for compressive strains

and lower for tensile strains. For z strain, the ReaxFF energies are larger than in DFT in general, showing an overestimation of the elastic modulus in the z direction. If we compare the level of discrepancy between ReaxFF and DFT here to the results of uniaxial strain for pristine MoS₂ in the 2017 parametrization (Fig. S5 in Ref.⁵⁶), we find the discrepancy is similar for the intercalated structures but larger for substituted structures.

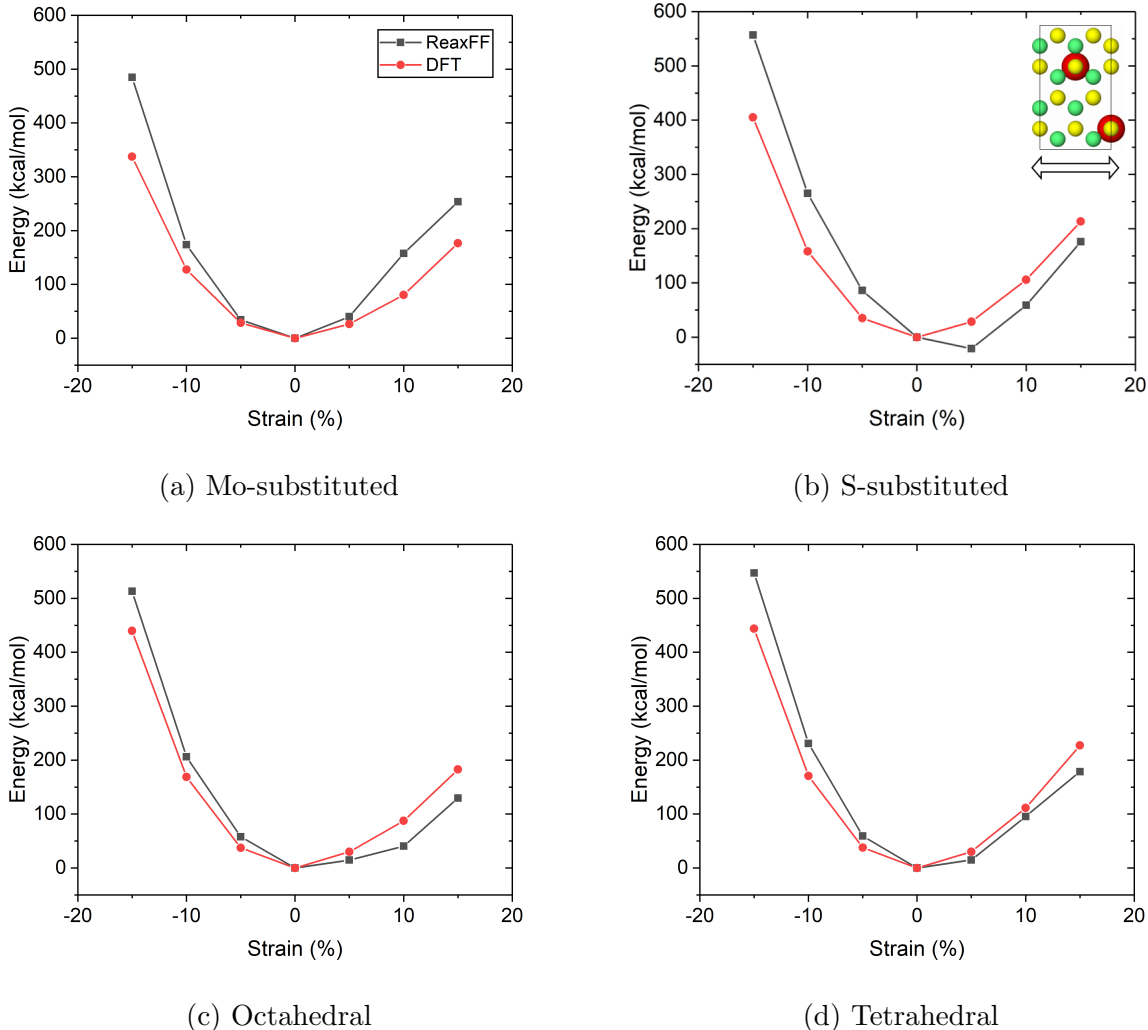
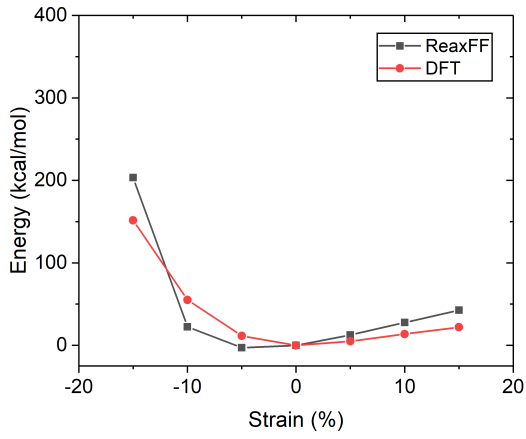
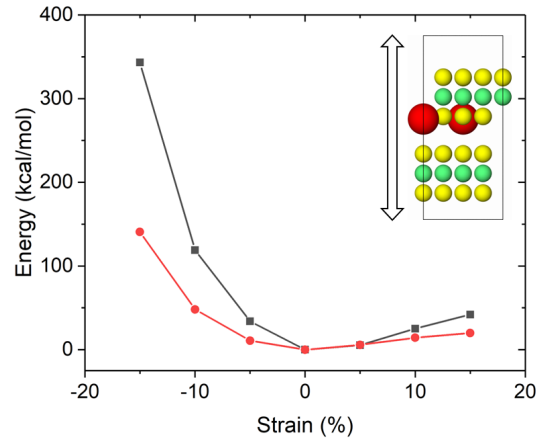


Figure 2: Equations of state calculated from DFT (red) and ReaxFF (black) for the Ni-doped MoS₂ structures strained uniaxially in the x -direction. The inset in (b) shows a top view of the S-substituted structure with an arrow indicating the strain direction.

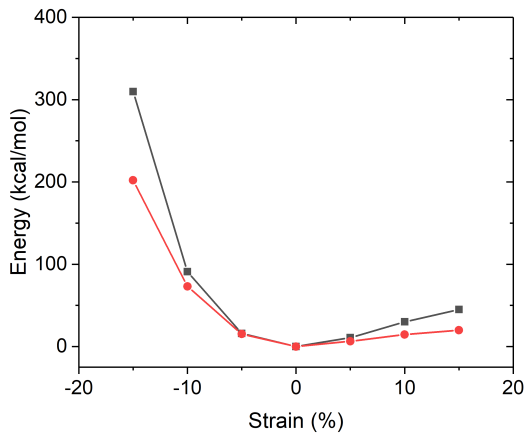
The results for biaxial and triaxial straining (where the specified strain value is applied to each axis) are shown in Figure 4 and 5, respectively, providing significantly better



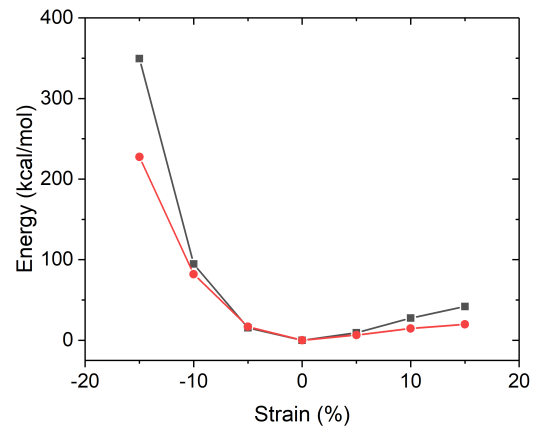
(a) Mo-substituted



(b) S-substituted



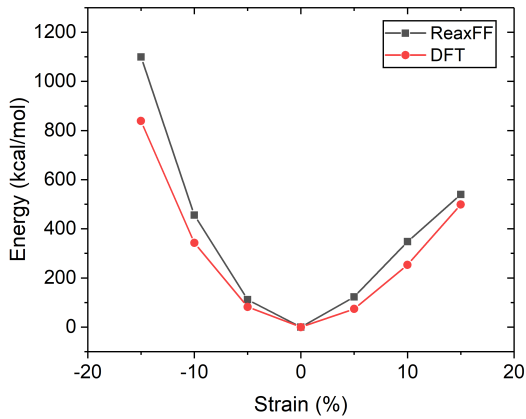
(c) Octahedral



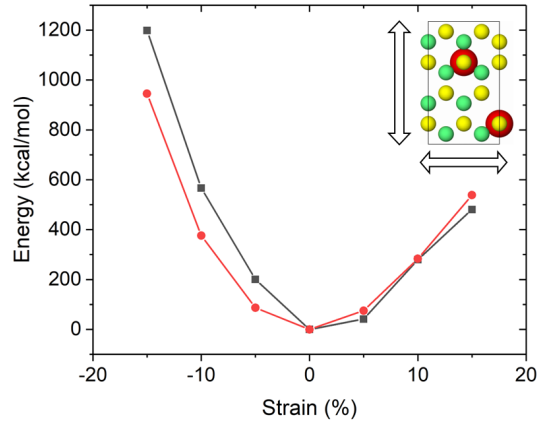
(d) Tetrahedral

Figure 3: Equations of state calculated from DFT (red) and ReaxFF (black) for the Ni-doped MoS_2 structures strained uniaxially in the z -direction. The inset in (b) shows a side view of the S-substituted structure with an arrow indicating the strain direction.

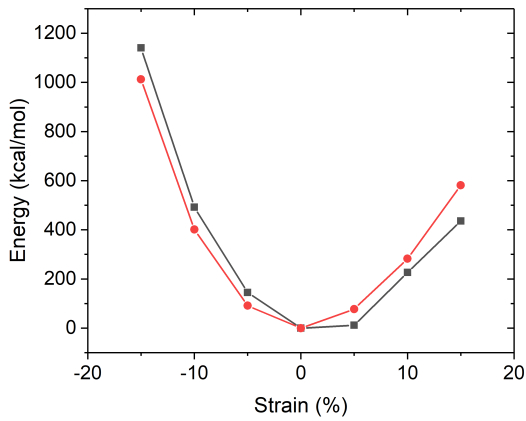
ReaxFF/DFT agreement than the uniaxial strain. We attribute the better agreement to the fact that bond angles change less in biaxial or triaxial strain than in uniaxial strain, so there is less dependence on the newly parametrized bond-angle terms in this work, and more dependence on the established Mo/S parameters we have taken from the literature. The energies as obtained from DFT calculations for the highest strains are ~ 1000 kcal/mol for biaxial strain and even higher (up to ~ 1800 kcal/mol) in the case of triaxial strain. Nevertheless, our force field is in good agreement with the DFT for the case of biaxial as well as triaxial straining. The ReaxFF energies are consistent with DFT for both the near-equilibrium structures and the far-from-equilibrium energies, and the energy minimum is correctly at zero strain (unlike in Fig. 3(a)).



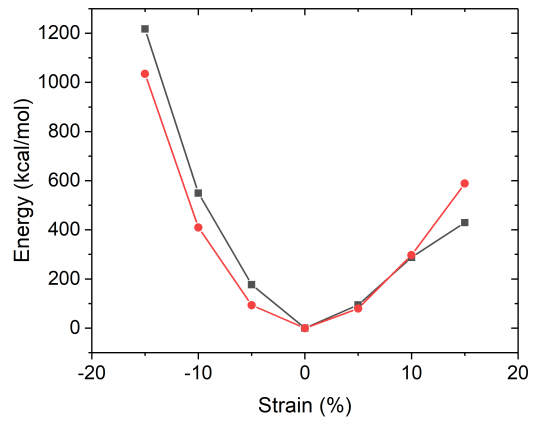
(a) Mo-substituted



(b) S-substituted



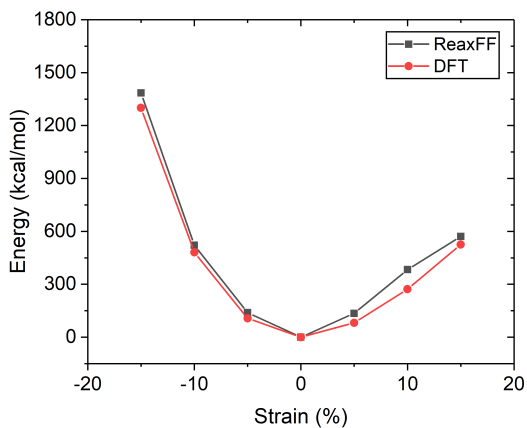
(c) Octahedral



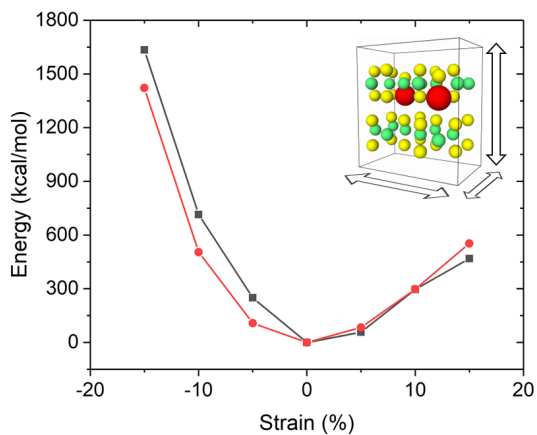
(d) Tetrahedral

Figure 4: Equations of state as obtained from DFT (red) and ReaxFF (black) for the Ni-doped MoS_2 structures strained biaxially for Mo-substituted, S-substituted, octahedral, and tetrahedral positions. The inset in (b) shows a top view of the S-substituted structure with two arrows indicating the strain directions.

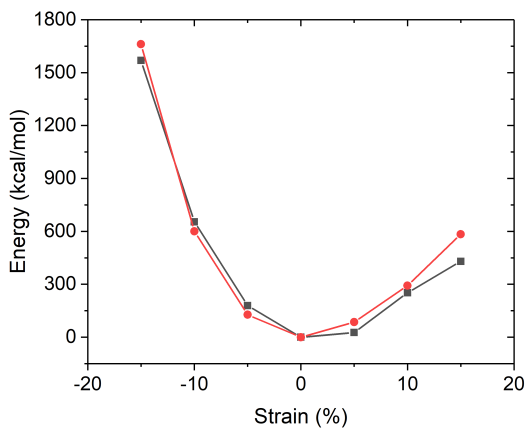
Finally, the ReaxFF energies for sheared structures were compared with DFT. Figure 6 shows excellent agreement for near-equilibrium as well as far-from-equilibrium structures. The minimum is correctly at 90° and the shape is close and correctly symmetrical. Mo-substituted has an overestimated shear modulus whereas S-substituted is very close, and octahedral and tetrahedral intercalation have an underestimated shear modulus.



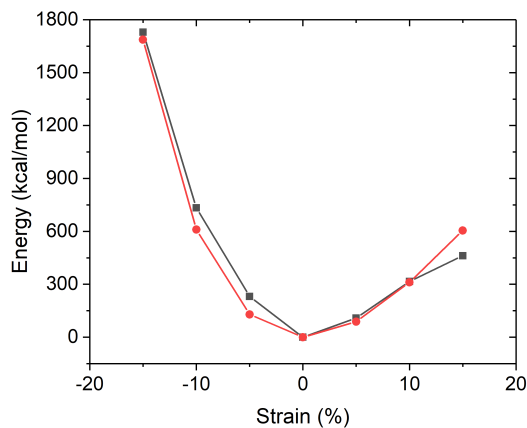
(a) Mo-substituted



(b) S-substituted



(c) Octahedral



(d) Tetrahedral

Figure 5: Equations of state as obtained from DFT (red) and ReaxFF (black) for the Ni-doped MoS_2 structures strained triaxially for Mo-substituted, S-substituted, octahedral, and tetrahedral positions. The inset in (b) shows a perspective view of the S-substituted structure with three arrows indicating the strain directions.

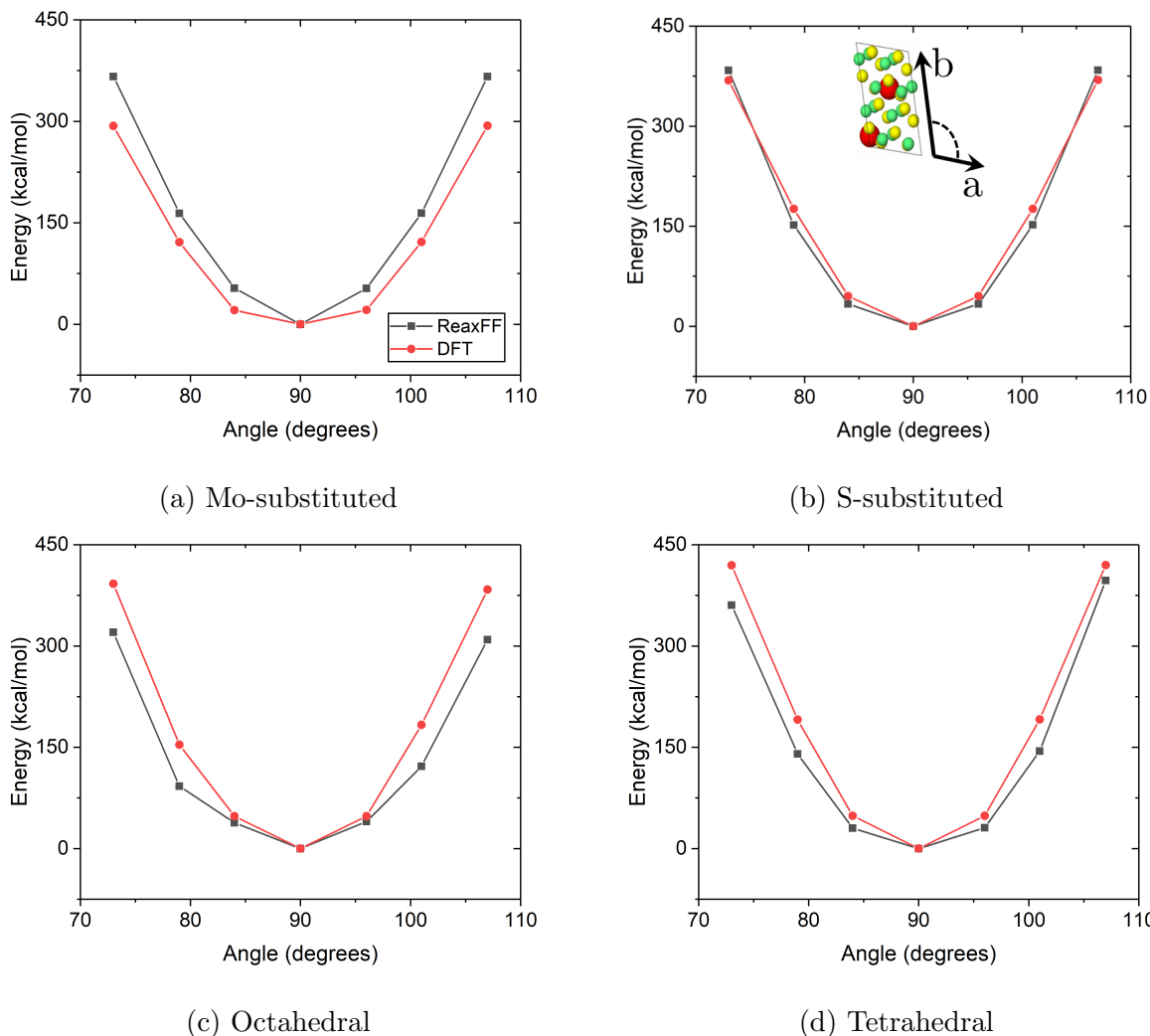


Figure 6: ReaxFF (black) and DFT (red) energies obtained for Ni-doped MoS_2 structures sheared in the xy basal plane for (a) Mo-substituted, (b) S-substituted, (c) octahedral, and (d) tetrahedral structures. The inset in (b) shows a top view of the basal plane of the S-substituted structure with arrows indicating the shearing angle as calculated from the angle between in-plane vectors a and b of the doubled cell.

Force Field Evaluation

Next we evaluated the force field's ability to predict parameters that were not included in the training. This evaluation was based on atom positions and distances obtained from relaxation of the model structures using energy minimization with the conjugate gradient algorithm with force and energy criteria of 10^{-6} kcal/mol-Å and 10^{-6} (unitless), respectively,

and a simulation of periodic cell optimization with a target zero stress tensor. First, the Ni–Mo and Ni–S atomic distances in all four structures were calculated. Results for Ni–Mo and Ni–S bond lengths are shown in Table 1a and 1b, respectively.

Table 1: Atomic distances (below 3.6 Å) between Ni and its neighbors from DFT and ReaxFF. Repeated distances are indicated with a multiplier.

Structure	DFT (Å)	ReaxFF (Å)
Mo-substituted	3.20×6	3.19×6
S-substituted	2.55×3	2.76×3
Octahedral	3.57×6	3.30/3.44/3.47–4.36/4.38/4.50
Tetrahedral	2.61×1	2.85×1

(a) Ni–Mo distances

Structure	DFT (Å)	ReaxFF (Å)
Mo-substituted	2.38×3	2.36×3
S-substituted	3.18×6	3.25×6
Octahedral	$2.34 \times 3, 2.38 \times 3$	2.24/2.24/2.37–2.83/3.04/3.09
Tetrahedral	$2.17 \times 3, 2.12 \times 1$	$2.32 \times 3, 2.27 \times 1$

(b) Ni–S distances

In most cases, the differences between ReaxFF and DFT bond lengths were within 0.1 Å, indicating the force field can accurately capture bond lengths within the Ni-doped MoS₂ structure. The same analysis for Mo–S bond lengths revealed that the difference between the DFT and ReaxFF calculated values was less than 0.1 Å for most cases and less than 0.2 Å for some cases in the octahedral and tetrahedral intercalation structures. For the pristine structure, the Mo–S bond length difference between DFT and ReaxFF calculated using the original 2022 parameters was 0.04Å. Generally, for Ni-doped MoS₂, ReaxFF predicted a slightly larger interlayer separation resulting an increase in the bond distances. The local symmetry around Ni, as shown by the multiplicity of the atomic distances, was correctly preserved in every case except the octahedral intercalation. However, for octahedral intercalation, the larger separation of the two MoS₂ layers in ReaxFF resulted in breaking of the symmetry that was predicted by DFT calculations, and much larger deviations in bond

lengths.

Next, the force field’s ability to reproduce Ni-doped MoS₂ structures with correct lattice parameters was tested. The parameters considered, illustrated in Figure 7, were the doubled cell vectors, a and b , the average distance h between S planes in a single layer, and the average interlayer separation d . The values for these parameters after structure relaxation in DFT and in ReaxFF are shown in Table 2. The d parameter decreases with doping for all structures in both ReaxFF and DFT, which is consistent with an experimentally measured reduction in c -parameter.⁸⁵ In most experiments, however, the atomistic structure of the Ni-doped MoS₂ is unknown, making precise comparisons between experiment and DFT unclear. The difference between the DFT- and ReaxFF-calculated parameters was less than 0.1 Å for most doped structures, as well as the pristine MoS₂ case which is shown for reference and relies only on the pre-existing Mo-S potential. This is consistent with the equation of state findings, since the optimized values of a and $c = 2h + 2d$ are the minima of the uniaxial x and z curves. The most notable discrepancy is for d in the octahedral case, where ReaxFF overestimates by ~ 0.4 Å.

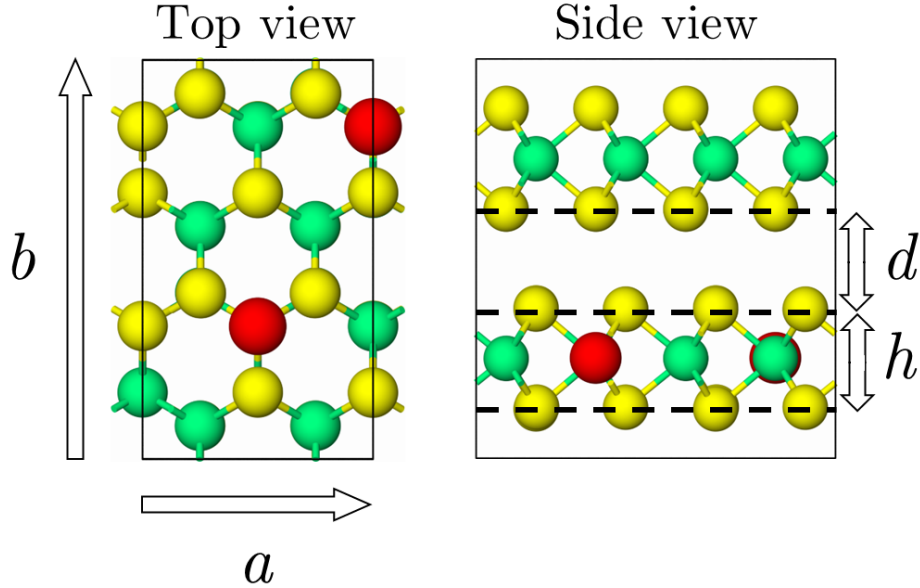


Figure 7: Structural parameters for Ni-doped MoS_2 illustrated for Mo-substituted configuration: cell vectors a and b , average distance h between S planes in a single layer, and average interlayer separation d .

Table 2: Comparison of structural parameters as obtained from DFT and ReaxFF for bulk Ni-doped MoS_2

Structure	a (Å)		b (Å)		d (Å)		h (Å)	
	DFT	ReaxFF	DFT	ReaxFF	DFT	ReaxFF	DFT	ReaxFF
Pristine	6.38	6.40	11.04	11.10	3.08	3.03	3.12	3.21
Mo-substituted	6.40	6.40	11.08	11.08	3.07	3.00	3.07	3.16
S-substituted	6.35	6.47	11.00	11.21	2.87	2.77	3.15	3.30
Octahedral	6.38	6.45	11.06	11.20	2.66	3.03	3.12	3.17
Tetrahedral	6.39	6.43	11.07	11.16	2.88	2.95	3.06	3.14

The accuracy of the developed force field was also tested in distinguishing the relative energies of Ni-doped 1H and 1T monolayer structures. We used 2×2 , 3×3 , and 4×4 in-plane supercells of the three-atom unit cell of 1H and 1T, where each supercell contained one Ni atom; these structures were then doubled to create orthogonal unit cells with two Ni atoms per cell. The different doping sites^{28,53} were: adatoms at the hollow position (three-fold

hollow space between top S atoms), Mo atop (on top of Mo), or S atop (on top of S); Mo-substituted, or S-substituted. The pristine structures were also included for reference, which had been studied in the 2017 work.⁵⁶ Note that neither 1H or 1T structures nor adatoms were in our training data. Snapshots of representative structures (S atop) of different sizes (doping concentrations) are shown in Figure 8. The energy differences between 1H and 1T polytypes were compared between ReaxFF and DFT in Figure 8, using DFT results from Karkee et al.²⁸ and Karkee and Strubbe⁵³. Results show that the force field can capture the energies corresponding to Ni dopants and adatoms with a small underestimation, as in the pristine case.⁵⁶

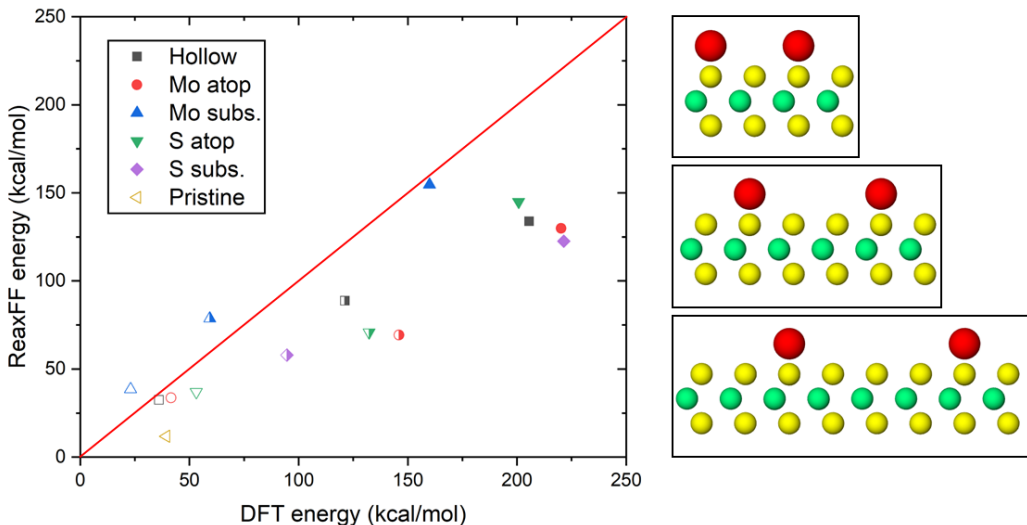


Figure 8: Energy difference between 1H and 1T polytypes for each structure of Ni-doped (or pristine) MoS_2 . Results show energy differences of the right scale for ReaxFF, but with less variation, leading to underestimation by ReaxFF for some doping locations. Change in the concentration from high to low is illustrated with open, half-filled, and solid symbols for 2×2 , 3×3 , and 4×4 supercells, respectively. Snapshots (right) show 2×2 , 3×3 , and 4×4 supercells of S atop site of 1H- MoS_2 (different size supercells correspond to different doping concentrations).

Given the prevalence of vacancies in real MoS_2 ⁸⁶ samples, and studies of vacancies with the 2017 ReaxFF potential,⁵⁶ we tested our reactive force field on defective bulk 2H structures

that combine Mo or S vacancies and Ni dopants. In each case, the vacancy was located at the nearest Mo or S site to the Ni dopant. Structures based on a $3 \times 3 \times 1$ supercell were constructed and underwent variable-cell relaxation in DFT, and then the DFT-relaxed structure was converted to a nearly orthorhombic doubled cell, imported to ReaxFF and relaxed using the developed force field. The goal to have an agreement between DFT and ReaxFF required that the final (i.e., after relaxation) atomic positions of Ni-doped MoS₂ atoms be the same (i.e., no structural changes during ReaxFF relaxation). A summary of atomic rearrangements during each relaxation is shown in Table 3.

Table 3: Summary of atomic rearrangements of 2H-MoS₂ with a Ni dopant and a vacancy, both at variable locations. In intercalations and S-substituted with a vacancy, Ni moves into the vacancy. All rearrangements predicted by DFT remain in ReaxFF.

Ni initial site	Vacancy initial site	Ni relaxed site	Vacancy relaxed site
Mo	Mo	Mo	Mo
Mo	S	Mo	S
S	Mo	Mo	S
S	S	S	S
Octahedral	Mo	Mo	-
Octahedral	S	S	-
Tetrahedral	Mo	Mo	-
Tetrahedral	S	S	-

Table 3 shows that, according to DFT, for the intercalated structures, Ni moved to the vacancy position, essentially converting an intercalated structure to a substituted structure (Mo-substituted for Ni filling an Mo vacancy and S-substituted for Ni filling an S vacancy). An example is shown in Fig. 9. This observation is consistent with the findings in Guerrero et al.²⁷ that the formation energy for tetrahedral intercalation in a $3 \times 3 \times 1$ supercell is 0.401 eV, greater than the energy for filling an Mo vacancy with Ni (-2.575 eV), and for filling an S vacancy (0.194 eV). The formation energy for octahedral intercalation is 0.9 eV higher, making the migration to a vacancy yet more exothermic. Since relaxation led to

the migrations, evidently these migrations have no barrier. We additionally observe that S-substituted Ni adjacent to an Mo vacancy moves to the Mo site, leaving behind an S vacancy. The ReaxFF relaxed structures preserved the same rearrangements as in DFT for all combinations of dopant and vacancy positions.

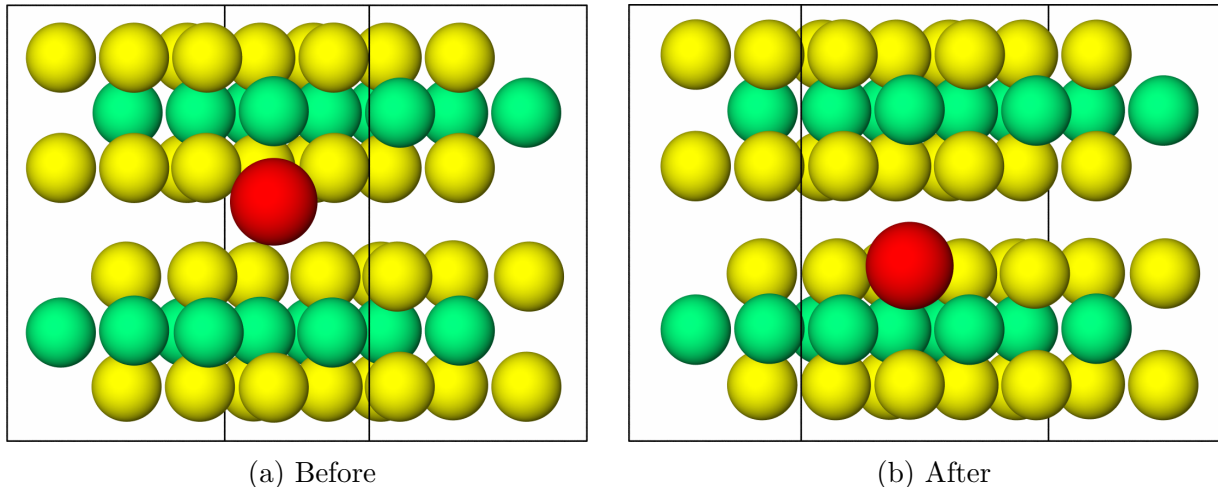


Figure 9: Relaxation of a dopant/vacancy structure as calculated by DFT: (a) tetrahedrally intercalated Ni adjacent to an S vacancy; (b) Ni has moved into the S site, forming S-substituted MoS₂.

Lastly, we evaluated the potential in terms of its ability to model interlayer sliding. Here, we rigidly displaced layers in the x - or y -directions, then relaxed in the z -direction, as in Guerrero and Strubbe⁵². However, as shown in Figs. S10-15, the sliding energies from ReaxFF did not match those from DFT, except for the Mo-substituted case sliding in the x -direction. In many cases, sliding leads to a reduction in energy in ReaxFF, i.e. an incorrect lowest-energy stacking is predicted vs. DFT. Even the original potentials could not capture sliding energies accurately (Figs. S12 and S15), since neither the original nor the doped potential was trained for sliding.

Simulations of Deposition and Annealing

To demonstrate the applicability of the newly developed force field, the process of sputter deposition and annealing to grow Ni-doped MoS₂ films⁸⁷ was simulated. The simulations

were performed using LAMMPS in the NVT ensemble with the Langevin thermostat, a damping parameter of 10.0 fs, and a time step of 0.1 fs. The simulation box was $2.5 \times 2.4 \times 10.0$ nm in the x -, y -, and z -directions, respectively, with periodic boundary conditions in the x - and y -directions. The boundary condition in the z -direction was fixed to mimic deposition in this direction. The initial configuration was a substrate consisting of bilayer 2H-MoS₂, with the bottommost layer held fixed during the simulation.

Atoms were deposited from 7.0 nm above the substrate surface, and a reflective virtual wall (which reflects downward only) was placed parallel to the surface at a distance of 4.8 nm to ensure deposited atoms remain near the substrate. The deposition process followed a simulation protocol used previously for SiO₂ thin film formation.⁸⁸ While the timescales accessible in atomistic simulations are much shorter than in real experiments, this kind of simulation has been found to be useful in generating realistic atomistic structures. First, energy minimization was performed to obtain the relaxed atomic positions, followed by thermal equilibration for 50 ps at room temperature. Next, Mo, S, and Ni atoms were continuously deposited onto the MoS₂ substrate at a 1:2 Mo to S ratio with Ni atoms replacing Mo atoms at 7% by weight, expected to promote Ni substitution for Mo.²³ The deposition rates for Mo and Ni were one atom every 40 fs with a deposition energy of 230 kcal/mol; for S atoms the deposition rate was one atoms every 20 fs with a deposition energy of 1.5 kcal/mol. Under typical experimental conditions, an inert gas such as argon is used to modulate the incident kinetics of the deposited Mo, S, and Ni radicals. Following previous simulations of Si-O deposition,⁸⁹ a lower deposition energy was used to slow the sulfur atoms such that they act not only as radicals but as kinetic energy modulators, without the need to explicitly model argon. The total number of deposited S, Mo, and Ni atoms after 50 ps was 1000, 405, and 95, respectively. At the end of the deposition process, the system was equilibrated at 300 K for 50 ps.

The second stage was annealing the deposited Ni-doped MoS₂ film, following a simulation process similar to that used previously for the crystallization of un-doped MoS₂.⁶² At this

stage, the constraints on the lowermost atoms were removed and the simulation cell height was set to the height of the reflective wall at 4.8 nm with the boundary condition in the z -direction changed to periodic to model bulk material. The annealing process was carried out by heating the model at the end of the deposition stage to 5000 K over 50 ps at a ramping rate of 100 K/ps. The structure was equilibrated at high temperature for 50 ps. Then, the structure was cooled to 2000 K at a rate of 30 K/ps followed by equilibration for 300 ps to trigger nucleation. Finally, the model was cooled to 300 K over 170 ps (10 K/ps).

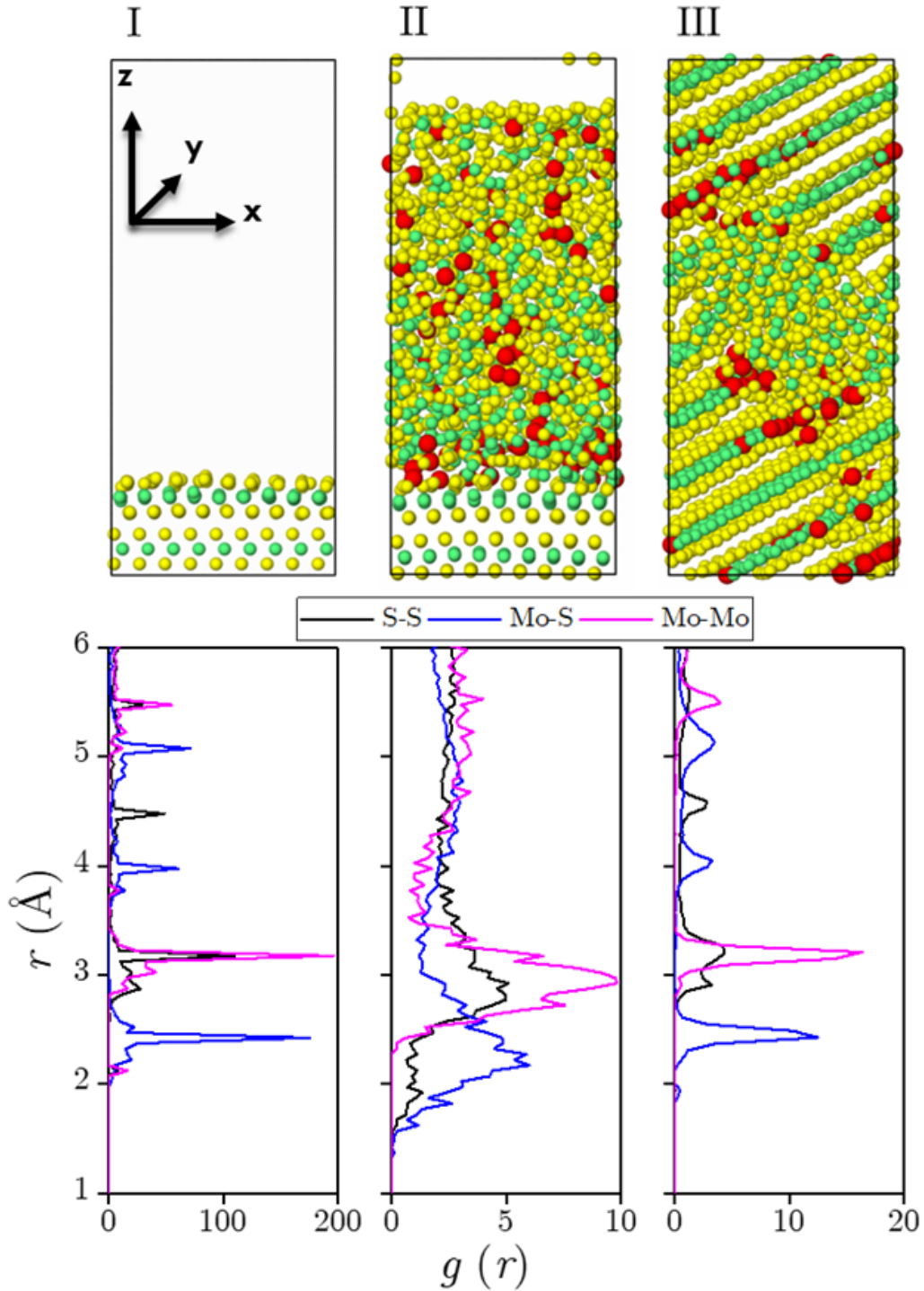


Figure 10: Side-view snapshots (top) and radial distribution function (bottom) of the model system, (I) before deposition, (II) at the end of the deposition, and (III) at the end of the annealing stage. A clear transition from amorphous to crystalline is observed (II) \rightarrow (III). Spheres represent S (yellow), Mo (green), and Ni (red) atoms. The black lines in the top snapshots correspond to the periodic boundaries of the cell during the annealing stage.

Snapshots of the model system before deposition, after deposition, and after annealing are shown in the top panel of Figure 10(I), (II), and (III), respectively. Visually, the model system appears amorphous at the end of deposition, consistent with experimental observations for magnetron-sputtered MoS₂,^{87,90} but then is mostly crystalline after annealing, as observed after annealing in experiments.^{87,90} Note that the middle region of the material (Figure 10(III)) does not appear crystalline from this view, but is in fact crystalline at an angle relative to the perspective shown here. An alternate angle from which the crystallinity of the entire model is visible is shown in Fig. S16. The crystallization process can be quantified using radial distribution functions (RDFs) of S–S, S–Mo, and Mo–Mo atom distances at the end of each stage of the simulation. The RDF of the initial crystal substrate after equilibration, shown in Figure 10(bottom panel (I)), exhibits clear peaks indicative of a perfect crystal. At the end of the deposition, Figure 10(bottom panel (II)) shows broad close-distance peaks and only weak further-distance (second neighbor) peaks, indicating an amorphous structure. Then, the RDF after annealing, shown in Figure 10(bottom panel (III)), has the regular peaks again, only slightly broadened from the before-deposition peaks, confirming that the material is in fact crystalline.

Visual analysis of the simulation after annealing suggested that most of the Ni atoms positioned themselves at Mo sites, resulting in a Mo-substituted Ni-doped MoS₂ structure. To confirm this, the distribution of Ni–S and Ni–Mo distances at the end of annealing are shown in Figure 11(b). The heights of the first Ni–S (red) peaks after annealing are at similar distances to those observed in Figure 11(a) for the Mo–S (red) peak. We can conclude that Ni atoms are bonded to S more than to Mo, consistent with the Mo-substituted Ni-doped MoS₂ structure. Previous DFT calculations have shown that, under S-rich conditions, Mo-substituted is the most favorable doping location for Ni.²⁷ Visual analysis of the post-annealing simulations also indicated that the Ni atoms were not randomly distributed throughout the crystal, but rather formed few-atom clusters. This observation is consistent with phase separation predicted for Mo substitution according to convex hull analysis of DFT

calculations.²⁷ Similar behavior has been previously observed for gold atoms co-sputtered with MoS₂,⁹¹ which is further support for the physical realism of these simulations and the new force field.

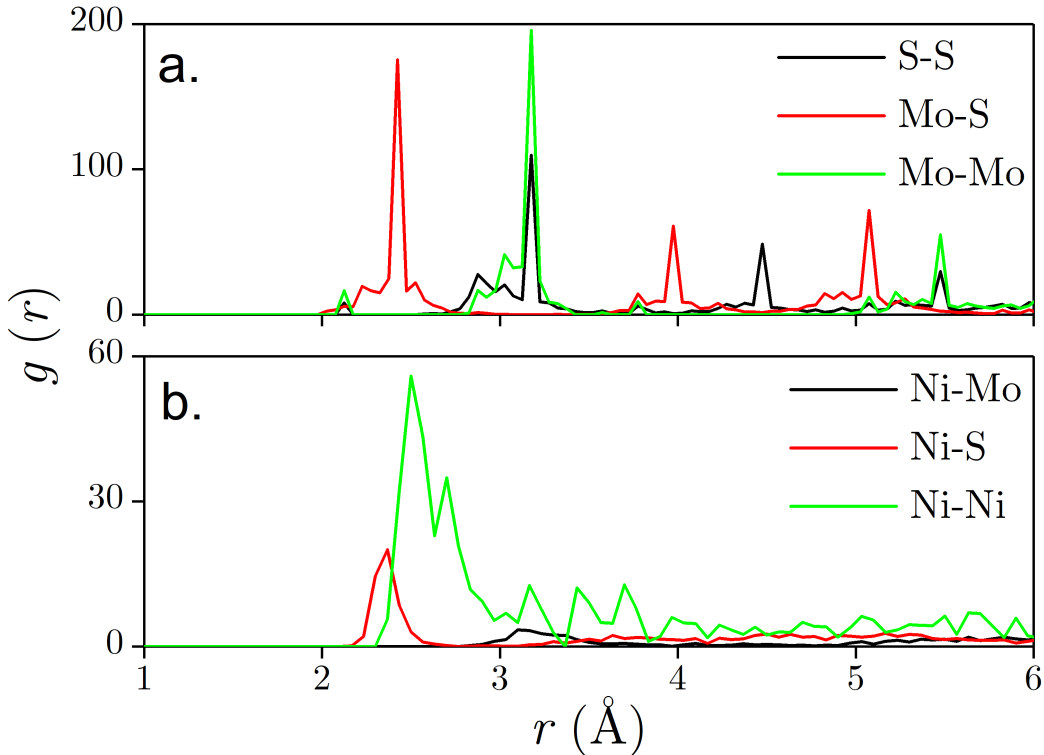


Figure 11: Radial distribution functions for (a) 2H MoS₂ substrate before deposition and (b) system after annealing. Similar peak locations for Ni-S and Mo-S, and for Ni-Mo and Mo-Mo, indicate occupation of Mo sites by Ni after annealing.

Conclusion

Two new ReaxFF force fields were developed for Ni-doped MoS₂. The force fields were developed by adding the parameters for Ni-Mo-S, Ni-S-Mo, and S-Ni-Mo angles to a previously optimized force field for MoS₂,^{56,62} and tuning those parameters to match DFT-calculated energies. The parameterization was based on strained DFT calculations of Mo-substituted, S-substituted, octahedral, and tetrahedral intercalation structures of the Ni dopant. Both force fields showed accurate and reliable results with the force field that was based on the

2022 parameters performing slightly better. Hence, the results from the 2022 parameters were shown in the main text. However, since the two original parameter sets were optimized for different MoS₂ models, i.e., single-layer versus bulk, the 2017 parameters' equation of state results were included in Figs. S5-S9. The final force field developed based on the 2022 potential was able to accurately predict the energy difference between tetrahedral and octahedral intercalation, lengths of Mo–Ni and S–Ni bonds, lattice constants, S–S distance, and interlayer separation. Furthermore, the developed force field agreed with DFT on the relaxed geometries of Ni-doped MoS₂ structures with vacancies. We note that the force field was not trained for interlayer sliding,⁵² and our initial testing indicates that it was not able to accurately capture sliding behavior for most dopant configurations; improvement of the force field to capture sliding energies could be considered in future work. To perform simulations relevant to catalysis with Ni-doped MoS₂, a next step would be to incorporate interactions with other elements like H. In addition, including torsion terms and training of the bond angle parameters that were taken from the literature might improve the accuracy of the force field. However, the force field is robust for modeling the crystal structures of Ni-doped MoS₂ and their elastic behavior, as well as the phase transition between amorphous and crystalline, and also the underlying mechanisms of doping. The ReaxFF force fields developed in this work will enable future simulation-based studies of the fundamental mechanisms by which Ni dopants affect MoS₂.

Supporting Information Available

Comparisons of the Ni/S and Mo/Ni force fields with DFT training data, comparison between ReaxFF and DFT equations of state with the force field developed based on the 2017 ReaxFF MoS₂ parameters,⁵⁶ sliding potentials for doped and pristine MoS₂ with 2017 and 2022 parameters, and alternate snapshot of the post-annealing doped material (PDF); relaxed structures from DFT (.POSCAR) and ReaxFF (.XYZ) and their minimized energies; and

ReaxFF parameter files (.txt) developed based on the 2017⁵⁶ and 2022⁶² MoS₂ parameters.

Acknowledgments

We acknowledge Rijan Karkee for providing Ni-doped 1T and 1H structures. Computing resources were provided by the Multi-Environment Computer for Exploration and Discovery (MERCED) cluster at UC Merced, funded by National Science Foundation Grant No. ACI-1429783, and the National Energy Research Scientific Computing Center (NERSC), a U.S. Department of Energy Office of Science User Facility operated under Contract No. DE-AC02-05CH11231. This work was supported by the Merced nAnomaterials Center for Energy and Sensing (MACES), a NASA-funded research and education center, under awards NNX15AQ01 and NNH18ZHA008CMIROG6R, and by UC Merced start-up funds.

References

- (1) Jaramillo, T. F.; Jørgensen, K. P.; Bonde, J.; Nielsen, J. H.; Horch, S.; Chorkendorff, I. Identification of active edge sites for electrochemical H₂ evolution from MoS₂ nanocatalysts. *Science* **2007**, *317*, 100–102.
- (2) Jeong, G.; Kim, C. H.; Hur, Y. G.; Han, G.-H.; Lee, S. H.; Lee, K.-Y. Ni-Doped MoS₂ Nanoparticles Prepared via Core–Shell Nanoclusters and Catalytic Activity for Upgrading Heavy Oil. *Energy Fuels* **2018**, *32*, 9263–9270.
- (3) Araki, Y.; Honna, K.; Shimada, H. Formation and catalytic properties of edge-bonded molybdenum sulfide catalysts on TiO₂. *J. Catal.* **2002**, *207*, 361–370.
- (4) Bhattacharya, D.; Mukherjee, S.; Mitra, R. K.; Ray, S. K. Size-dependent optical properties of MoS₂ nanoparticles and their photo-catalytic applications. *Nanotechnology* **2020**, *31*, 145701.

- (5) Deng, J.; Li, H.; Xiao, J.; Tu, Y.; Deng, D.; Yang, H.; Tian, H.; Li, J.; Ren, P.; Bao, X. Triggering the electrocatalytic hydrogen evolution activity of the inert two-dimensional MoS₂ surface *via* single-atom metal doping. *Energy Environ. Sci.* **2015**, *8*, 1594–1601.
- (6) Zong, X.; Na, Y.; Wen, F.; Ma, G.; Yang, J.; Wang, D.; Ma, Y.; Wang, M.; Sun, L.; Li, C. Visible light driven H₂ production in molecular systems employing colloidal MoS₂ nanoparticles as catalyst. *Chem. Commun.* **2009**, *30*, 4536–4538.
- (7) Cuddy, M. J.; Arkill, K. P.; Wang, Z. W.; Komsa, H. P.; Krashennnikov, A. V.; Palmer, R. E. Fabrication and atomic structure of size-selected, layered MoS₂ clusters for catalysis. *Nanoscale* **2014**, *6*, 12463–12469.
- (8) Mao, J.; Wang, Y.; Zheng, Z.; Deng, D. The rise of two-dimensional MoS₂ for catalysis. *Front. Phys.* **2018**, *13*, 138118.
- (9) Kumari, S.; Gusain, R.; Kumar, A.; Manwar, N.; Jain, S. L.; Khatri, O. P. Direct growth of nanostructural MoS₂ over the *h*-BN nanoplatelets: an efficient heterostructure for visible light photoreduction of CO₂ to methanol. *J. CO₂ Util.* **2020**, *42*, 101345.
- (10) Li, Y.; Tang, J.; Wei, Y.; He, W.; Tang, Z.; Zhang, X.; Xiong, J.; Zhao, Z. The heterojunction between 3D ordered macroporous TiO₂ and MoS₂ nanosheets for enhancing visible-light driven CO₂ reduction. *J. CO₂ Util.* **2021**, *51*, 101648.
- (11) Chen, W.; Liu, M.; Wei, S.; Li, X.; Mao, L.; Shangguan, W. Solid-state synthesis of ultrathin MoS₂ as a cocatalyst on mesoporous g-C₃N₄ for excellent enhancement of visible light photoactivity. *J. Alloys Compd.* **2020**, *836*, 155401.
- (12) Radisavljevic, B.; Radenovic, A.; Brivio, J.; Giacometti, V.; Kis, A. Single-layer MoS₂ transistors. *Nat. Nanotechnol.* **2011**, *6*, 147–150.
- (13) Yuan, H.; Cheng, G.; You, L.; Li, H.; Zhu, H.; Li, W.; Kopanski, J. J.; Obeng, Y. S.; Hight Walker, A. R.; Gundlach, D. J. et al. Influence of metal–MoS₂ interface on MoS₂

- transistor performance: comparison of Ag and Ti contacts. *ACS Appl. Mater. Interfaces* **2015**, *7*, 1180–1187.
- (14) van der Zande, A. M.; Huang, P. Y.; Chenet, D. A.; Berkelbach, T. C.; You, Y.; Lee, G.-H.; Heinz, T. F.; Reichman, D. R.; Muller, D. A.; Hone, J. C. Grains and grain boundaries in highly crystalline monolayer molybdenum disulphide. *Nat. Mater.* **2013**, *12*, 554–561.
- (15) Vazirisereshk, M. R.; Martini, A.; Strubbe, D. A.; Baykara, M. Z. Solid lubrication with MoS₂: a review. *Lubricants* **2019**, *7*, 57.
- (16) Domínguez-Meister, S.; Rojas, T. C.; Brizuela, M.; Sánchez-López, J. C. Solid lubricant behavior of MoS₂ and WSe₂-based nanocomposite coatings. *Sci. Technol. Adv. Mater.* **2017**, *18*, 122–133.
- (17) Guo, J.; Peng, R.; Du, H.; Shen, Y.; Li, Y.; Li, J.; Dong, G. The application of nano-MoS₂ quantum dots as liquid lubricant additive for tribological behavior improvement. *Nanomaterials* **2020**, *10*, 200.
- (18) Mousavi, S. B.; Heris, S. Z.; Estellé, P. Experimental comparison between ZnO and MoS₂ nanoparticles as additives on performance of diesel oil-based nano lubricant. *Sci. Rep.* **2020**, *10*, 5813.
- (19) Lauritsen, J.; Kibsgaard, J.; Olesen, G.; Moses, P.; Hinnemann, B.; Helveg, S.; Nørskov, J. K.; Clausen, B. S.; Topsøe, H.; Lægsgaard, E. et al. Location and coordination of promoter atoms in Co- and Ni-promoted MoS₂-based hydrotreating catalysts. *J. Catal.* **2007**, *249*, 220–233.
- (20) Zhang, D.; Wu, J.; Li, P.; Cao, Y. Room-temperature SO₂ gas-sensing properties based on a metal-doped MoS₂ nanoflower: an experimental and density functional theory investigation. *J. Mater. Chem. A* **2017**, *5*, 20666–20677.

- (21) Ko, T.; Huang, C.; Lin, D.; Ruan, Y.; Huang, Y. Electrical and optical properties of Co-doped and undoped MoS₂. *Jpn. J. Appl. Phys.* **2016**, *55*, 04EP06.
- (22) Xie, Y.; Li, Y. Preparation of Ni-doped MoS₂ microsphere and its superior electrocatalytic hydrogen evolution ability. *Adv. Mater. Res.* **2014**, *871*, 206–210.
- (23) Vellore, A.; Romero Garcia, S.; Walters, N.; Johnson, D.; Kennett, A.; Heverly, M.; Martini, A. Ni-doped MoS₂ dry film lubricant life. *Adv. Mater. Interfaces* **2020**, *7*, 2001109.
- (24) Acikgoz, O.; Guerrero, E.; Yanilmaz, A.; Dagdeviren, O. E.; Çelebi, C.; Strubbe, D. A.; Baykara, M. Z. Intercalation leads to inverse layer dependence of friction on chemically doped MoS₂. *Nanotechnology* **2023**, *34*, 015706.
- (25) Kong, X.; Wang, N.; Zhang, Q.; Liang, J.; Wang, M.; Wei, C.; Chen, X.; Zhao, Y.; Zhang, X. Ni-doped MoS₂ as an efficient catalyst for electrochemical hydrogen evolution in alkaline media. *ChemistrySelect* **2018**, *3*, 9493–9498.
- (26) Rajendhran, N.; Palanisamy, S.; Periyasamy, P.; Venkatachalam, R. Enhancing of the tribological characteristics of the lubricant oils using Ni-promoted MoS₂ nanosheets as nano-additives. *Tribol. Int.* **2018**, *118*, 314–328.
- (27) Guerrero, E.; Karkee, R.; Strubbe, D. A. Phase stability and Raman/IR signatures of Ni-doped MoS₂ from DFT studies. *J. Phys. Chem. C* **2021**, *125*, 13401–13412.
- (28) Karkee, R.; Guerrero, E.; Strubbe, D. A. Enhanced interlayer interactions in Ni-doped MoS₂, and structural and electronic signatures of doping site. *Phys. Rev. Materials* **2021**, *5*, 074006.
- (29) Kondekar, N.; Boebinger, M. G.; Tian, M.; Kirmani, M. H.; McDowell, M. T. The effect of nickel on MoS₂ growth revealed with in situ transmission electron microscopy. *ACS Nano* **2019**, *13*, 7117–7126.

- (30) Pan, U. N.; Singh, T. I.; Paudel, D. R.; Gudal, C. C.; Kim, N. H.; Lee, J. H. Covalent doping of Ni and P on 1T-enriched MoS₂ bifunctional 2D-nanostructures with active basal planes and expanded interlayers boosts electrocatalytic water splitting. *J. Mater. Chem. A* **2020**, *8*, 19654–19664.
- (31) Jiang, Y.; Li, S.; Zhang, F.; Zheng, W.; Zhao, L.; Feng, Q. Metal-semiconductor 1T/2H-MoS₂ by a heteroatom-doping strategy for enhanced electrocatalytic hydrogen evolution. *Catal. Commun.* **2021**, *156*, 106325.
- (32) Geng, D.; Bo, X.; Guo, L. Ni-doped molybdenum disulfide nanoparticles anchored on reduced graphene oxide as novel electroactive material for a non-enzymatic glucose sensor. *Sens. Actuators B Chem.* **2017**, *244*, 131–141.
- (33) Escalera-López, D.; Niu, Y.; Yin, J.; Cooke, K.; Rees, N. V.; Palmer, R. E. Enhancement of the hydrogen evolution reaction from Ni-MoS₂ hybrid nanoclusters. *ACS Catal.* **2016**, *6*, 6008–6017.
- (34) Wang, D.; Zhang, X.; Shen, Y.; Wu, Z. Ni-doped MoS₂ nanoparticles as highly active hydrogen evolution electrocatalysts. *RSC Adv.* **2016**, *6*, 16656–16661.
- (35) Zhang, J.; Wang, T.; Liu, P.; Liu, S.; Dong, R.; Zhuang, X.; Chen, M.; Feng, X. Engineering water dissociation sites in MoS₂ nanosheets for accelerated electrocatalytic hydrogen production. *Energy Environ. Sci.* **2016**, *9*, 2789–2793.
- (36) Xu, J.; Shao, G.; Tang, X.; Lv, F.; Xiang, H.; Jing, C.; Liu, S.; Dai, S.; Li, Y.; Luo, J. et al. Frenkel-defected monolayer MoS₂ catalysts for efficient hydrogen evolution. *Nat. Commun.* **2022**, *13*, 1–8.
- (37) Dong, T.; Zhang, X.; Wang, P.; Chen, H.-S.; Yang, P. Formation of Ni-doped MoS₂ nanosheets on N-doped carbon nanotubes towards superior hydrogen evolution. *Electrochim. Acta* **2020**, *338*, 135885.

- (38) Khan, M.; Hasan, M.; Bhatti, K.; Rizvi, H.; Wahab, A.; Rehman, S.-u.; Afzal, M. J.; Nazneen, A.; Nazir, A.; Iqbal, M. et al. Effect of Ni doping on the structural, optical and photocatalytic activity of MoS₂, prepared by Hydrothermal method. *Mater. Res. Express* **2020**, *7*, 015061.
- (39) Xuan, N.; Chen, J.; Shi, J.; Yue, Y.; Zhuang, P.; Ba, K.; Sun, Y.; Shen, J.; Liu, Y.; Ge, B. et al. Single-atom electroplating on two dimensional materials. *Chem. Mater.* **2018**, *31*, 429–435.
- (40) Zhang, R.; Dong, Y.; Al-Tahan, M. A.; Zhang, Y.; Wei, R.; Ma, Y.; Yang, C.; Zhang, J. Insights into the sandwich-like ultrathin Ni-doped MoS₂/rGO hybrid as effective sulfur hosts with excellent adsorption and electrocatalysis effects for lithium-sulfur batteries. *J. Energy Chem.* **2021**, *60*, 85–94.
- (41) Jenisha, M. A.; Kavirajan, S.; Harish, S.; Archana, J.; Kamalabharathi, K.; Kumar, E. S.; Navaneethan, M. Interfacial engineering effect and bipolar conduction of Ni-doped MoS₂ nanostructures for thermoelectric application. *J. Alloys Compd.* **2022**, *895*, 162493.
- (42) Stupp, B. C. Synergistic effects of metals co-sputtered with MoS₂. *Thin Solid Films* **1981**, *84*, 257–266.
- (43) Rajendhran, N.; Palanisamy, S.; Periyasamy, P.; Venkatachalam, R. Enhancing of the tribological characteristics of the lubricant oils using Ni-promoted MoS₂ nanosheets as nano-additives. *Tribol. Int.* **2018**, *118*, 314–328.
- (44) Zabinski, J. S.; Donley, M. S.; Walck, S. D.; Schneider, T. R.; McDevitt, N. T. The effects of dopants on the chemistry and tribology of sputter-deposited MoS₂ films. *Tribol. Trans.* **1995**, *38*, 894–904.
- (45) Hamilton, M. A.; Alvarez, L. A.; Mauntler, N. A.; Argibay, N.; Colbert, R.; Burris, D. L.; Muratore, C.; Voevodin, A. A.; Perry, S. S.; Sawyer, W. G. A possible

- link between macroscopic wear and temperature dependent friction behaviors of MoS₂ coatings. *Tribol. Lett.* **2008**, *32*, 91–98.
- (46) Zou, T. Z.; Tu, J. P.; Zhang, S. C.; Chen, L. M.; Wang, Q.; Zhang, L. L.; He, D. N. Friction and wear properties of electroless Ni-P-(IF-MoS₂) composite coatings in humid air and vacuum. *Mater. Sci. Eng. A* **2006**, *426*, 162–168.
- (47) Wang, H.; Tsai, C.; Kong, D.; Chan, K.; Abild-Pedersen, F.; Nørskov, J.; Cui, Y. Transition-metal doped edge sites in vertically aligned MoS₂ catalysts for enhanced hydrogen evolution. *Nano Res.* **2015**, *8*, 566–575.
- (48) Wei, H.; Gui, Y.; Kang, J.; Wang, W.; Tang, C. A DFT study on the adsorption of H₂S and SO₂ on Ni doped MoS₂ monolayer. *Nanomaterials* **2018**, *8*, 646.
- (49) Ma, D.; Ju, W.; Li, T.; Zhang, X.; He, C.; Ma, B.; Lu, Z.; Yang, Z. The adsorption of CO and NO on the MoS₂ monolayer doped with Au, Pt, Pd, or Ni: a first-principles study. *Appl. Surf. Sci.* **2016**, *383*, 98–105.
- (50) Raybaud, P.; Hafner, J.; Kresse, G.; Kasztelan, S.; Toulhoat, H. Structure, energetics, and electronic properties of the surface of a promoted MoS₂ catalyst: an ab initio local density functional study. *J. Catal.* **2000**, *190*, 128–143.
- (51) Hao, Y.; Wang, Y.-T.; Xu, L.-C.; Yang, Z.; Liu, R.-p.; Li, X.-y. 1T-MoS₂ monolayer doped with isolated Ni atoms as highly active hydrogen evolution catalysts: a density functional study. *Appl. Surf. Sci.* **2019**, *469*, 292–297.
- (52) Guerrero, E.; Strubbe, D. A. Atomistic Mechanisms of Sliding in Few-Layer and Bulk Doped MoS₂. *arXiv:2209.15629* **2022**, submitted 30 Sept 2022, <https://doi.org/10.48550/arXiv.2209.15629>.
- (53) Karkee, R.; Strubbe, D. A. Panoply of doping-induced reconstructions and elec-

- tronic phases in Ni-doped 1T-MoS₂. *arXiv:2107.07541* **2022**, submitted 11 Mar 2022, <https://doi.org/10.48550/arXiv.2107.07541>.
- (54) Jiang, J.-W.; Park, H. S.; Rabczuk, T. Molecular dynamics simulations of single-layer molybdenum disulphide (MoS₂): Stillinger-Weber parametrization, mechanical properties, and thermal conductivity. *J. Appl. Phys.* **2013**, *114*, 064307.
- (55) Jiang, J.-W.; Zhou, Y.-P. In *Handbook of Stillinger-Weber Potential Parameters for Two-Dimensional Atomic Crystals*; Jiang, J.-W., Zhou, Y.-P., Eds.; IntechOpen: Rijeka, 2017; Chapter 1.
- (56) Ostadhosseini, A.; Rahnamoun, A.; Wang, Y.; Zhao, P.; Zhang, S.; Crespi, V. H.; van Duin, A. C. ReaxFF reactive force-field study of molybdenum disulfide (MoS₂). *J. Phys. Chem. Lett.* **2017**, *8*, 631–640.
- (57) Liu, J.; Zeng, J.; Zhu, C.; Miao, J.; Huang, Y.; Heinz, H. Interpretable molecular models for molybdenum disulfide and insight into selective peptide recognition. *Chem. Sci.* **2020**, *33*, 8708.
- (58) Xing, J.; Shi, H.; Li, Y.; Liu, J. Molecular dynamics study of Cr doping on the crystal structure and surficial/interfacial properties of 2H-MoS₂. *Phys. Chem. Chem. Phys.* **2022**, *24*, 4547.
- (59) Liang, T.; Phillpot, S. R.; Sinnott, S. B. Parametrization of a reactive many-body potential for Mo–S systems. *Phys. Rev. B* **2009**, *79*, 245110.
- (60) Hong, S.; Krishnamoorthy, A.; Rajak, P.; Tiwari, S.; Misawa, M.; Shimojo, F.; Kalia, R.; Nakano, A.; Vashishta, P. Computational synthesis of MoS₂ layers by reactive molecular dynamics simulations: initial sulfidation of MoO₃ surfaces. *Nano Lett.* **2017**, *17*, 4866–4872.

- (61) Chen, R.; Jusufi, A.; Schilowitz, A.; Martini, A. Formation of MoS₂ from elemental Mo and S using reactive molecular dynamics simulations. *J. Vac. Sci. Technol. A* **2020**, *38*, 022201.
- (62) Ponomarev, I.; Polcar, T.; Nicolini, P. New Reactive Force Field for Simulations of MoS₂ Crystallization. *J. Phys. Chem. C* **2022**, *126*, 9475–9481.
- (63) Chen, R.; Konicek, A. R.; Jusufi, A.; Kliewer, C. E.; Jaishankar, A.; Schilowitz, A.; Martini, A. Limiting domain size of MoS₂: effects of stoichiometry and oxygen. *J. Phys. Chem. C* **2020**, *124*, 27571–27579.
- (64) Hu, G.; Fung, V.; Sang, X.; Unocic, R. R.; Ganesh, P. Predicting synthesizable multifunctional edge reconstructions in two-dimensional transition metal dichalcogenides. *npj Comput. Mater.* **2020**, *6*, 1–9.
- (65) Yilmaz, D. E.; Lotfi, R.; Ashraf, C.; Hong, S.; van Duin, A. C. Defect design of two-dimensional MoS₂ structures by using a graphene layer and potato stamp concept. *J. Phys. Chem. C* **2018**, *122*, 11911–11917.
- (66) Noori, H.; Mortazavi, B.; Keshtkari, L.; Zhuang, X.; Rabczuk, T. Nanopore creation in MoS₂ and graphene monolayers by nanoparticles impact: a reactive molecular dynamics study. *Appl. Phys. A* **2021**, *127*, 1–13.
- (67) Patra, T. K.; Zhang, F.; Schulman, D. S.; Chan, H.; Cherukara, M. J.; Terrones, M.; Das, S.; Narayanan, B.; Sankaranarayanan, S. K. Defect dynamics in 2-D MoS₂ probed by using machine learning, atomistic simulations, and high-resolution microscopy. *ACS Nano* **2018**, *12*, 8006–8016.
- (68) Zahedi, R. K.; Alajlan, N.; Zahedi, H. K.; Rabczuk, T. Mechanical properties of all MoS₂ monolayer heterostructures: crack propagation and existing notch study. *Comput. Mater. Contin.* **2022**, *70*, 4635–4655.

- (69) Mejía-Rosales, S.; Sandoval-Salazar, S. A.; Soria-Sánchez, A.; Cantú-Sánchez, L. Y. Mechanical properties of MoS₂ nanotubes under tension: a molecular dynamics study. *Mol. Simul.* **2021**, *47*, 471–479.
- (70) Mortazavi, B.; Ostadhossein, A.; Rabczuk, T.; Van Duin, A. C. T. Mechanical response of all-MoS₂ single-layer heterostructures: a ReaxFF investigation. *Phys. Chem. Chem. Phys.* **2016**, *18*, 23695–23701.
- (71) Shi, Y.; Cai, Z.; Pu, J.; Wang, L.; Xue, Q. Interfacial molecular deformation mechanism for low friction of MoS₂ determined using ReaxFF-MD simulation. *Ceram. Int.* **2019**, *45*, 2258–2265.
- (72) Giannozzi, P.; Andreussi, O.; Brumme, T.; Bunau, O.; Buongiorno Nardelli, M.; Calandra, M.; Car, R.; Cavazzoni, C.; Ceresoli, D.; Cococcioni, M. et al. Advanced capabilities for materials modelling with QUANTUM ESPRESSO. *J. Phys. Condens. Matter* **2017**, *29*, 465901.
- (73) Perdew, J. P.; Burke, K.; Ernzerhof, M. Generalized Gradient Approximation made simple. *Phys. Rev. Lett.* **1996**, *77*, 3865–3868.
- (74) Grimme, S. Semiempirical GGA-type density functional constructed with a long-range dispersion correction. *J. Comput. Chem.* **2006**, *27*, 1787–1799.
- (75) Hamann, D. R. Optimized norm-conserving Vanderbilt pseudopotentials. *Phys. Rev. B* **2013**, *88*, 085117.
- (76) Schlipf, M.; Gygi, F. Optimization algorithm for the generation of ONCV pseudopotentials. *Comput. Phys. Commun.* **2015**, *196*, 36–44.
- (77) van Duin, A. C.; Dasgupta, S.; Lorant, F.; Goddard, W. A. ReaxFF: a reactive force field for hydrocarbons. *J. Phys. Chem. A* **2001**, *105*, 9396–9409.

- (78) Vasenkov, A.; Newsome, D.; Verners, O.; Russo Jr, M. F.; Zaharieva, R.; Van Duin, A. C. T. Reactive molecular dynamics study of Mo-based alloys under high-pressure, high-temperature conditions. *J. Appl. Phys.* **2012**, *112*, 013511.
- (79) Mueller, J. E.; van Duin, A. C.; Goddard III, W. A. Development and validation of ReaxFF reactive force field for hydrocarbon chemistry catalyzed by nickel. *J. Phys. Chem. C* **2010**, *114*, 4939–4949.
- (80) van Duin, A. C. T.; Baas, J. M. A.; Van De Graaf, B. Delft molecular mechanics: a new approach to hydrocarbon force fields. Inclusion of a geometry-dependent charge calculation. *J. Chem. Soc., Faraday Trans.* **1994**, *90*, 2881–2895.
- (81) Hahn, S. H.; Rimsza, J.; Criscenti, L.; Sun, W.; Deng, L.; Du, J.; Liang, T.; Sinnott, S. B.; Van Duin, A. C. T. Development of a ReaxFF reactive force field for NaSiO_x/water systems and its application to sodium and proton self-diffusion. *J. Phys. Chem. C* **2018**, *122*, 19613–19624.
- (82) Nayir, N.; Van Duin, A. C. T.; Erkoc, S. Development of the ReaxFF reactive force field for inherent point defects in the Si/silica system. *J. Phys. Chem. A* **2019**, *123*, 4303–4313.
- (83) Khajeh, A.; Hu, X.; Mohammadtabar, K.; Shin, Y.; van Duin, A. C. .; Berkebile, S.; Martini, A. Statistical analysis of tri-cresyl phosphate conversion on an iron oxide surface using reactive molecular dynamics simulations. *J. Phys. Chem. C* **2019**, *123*, 12886–12893.
- (84) Plimpton, S. Fast parallel algorithms for short-range molecular dynamics. *J. Comput. Phys.* **1995**, *117*, 1–19.
- (85) Garreau, F. B.; Toulhoat, H.; Kasztelan, S.; Paulus, R. Low-Temperature Synthesis of Mixed NiMo Sulfides: Structural, Textural, and Catalytic Properties. *Polyhedron* **1986**, *5*, 211–217.

- (86) Zhou, W.; Zou, X.; Najmaei, S.; Liu, Z.; Shi, Y.; Kong, J.; Lou, J.; Ajayan, P. M.; Yakobson, B. I.; Idrobo, J.-C. Intrinsic structural defects in monolayer molybdenum disulfide. *Nano Lett.* **2013**, *13*, 2615–2622.
- (87) Sirota, B.; Glavin, N.; Voevodin, A. A. Room temperature magnetron sputtering and laser annealing of ultrathin MoS₂ for flexible transistors. *Vacuum* **2019**, *160*, 133–138.
- (88) Taguchi, M.; Hamaguchi, S. MD simulations of amorphous SiO₂ thin film formation in reactive sputtering deposition processes. *Thin Solid Films* **2007**, *515*, 4879–4882.
- (89) Grigoriev, F. V.; Sulimov, A. V.; Kochikov, I.; Kondakova, O. A.; Sulimov, V. B.; Tikhonravov, A. V. High-performance atomistic modeling of optical thin films deposited by energetic processes. *Int. J. High Perform. Comput. Appl.* **2015**, *29*, 184–192.
- (90) McConney, M. E.; Glavin, N. R.; Juhl, A. T.; Check, M. H.; Durstock, M. F.; Voevodin, A. A.; Shelton, T. E.; Bultman, J. E.; Hu, J.; Jespersen, M. L. et al. Direct synthesis of ultra-thin large area transition metal dichalcogenides and their heterostructures on stretchable polymer surfaces. *J. Mater. Res.* **2016**, *31*, 967–974.
- (91) Scharf, T. W.; Goeke, R. S.; Kotula, P. G.; Prasad, S. V. Synthesis of Au-MoS₂ nanocomposites: thermal and friction-induced changes to the structure. *ACS Appl. Mater. Interfaces* **2013**, *5*, 11762–11767.

TOC Graphic

